

## Effects of 3D Microstructural Distribution on Short Crack Growth Behavior in two Bimodal Ti-6Al-4V Alloys

Hassanipour, M.  
Department of Mechanical Engineering, Kyushu University

Watanabe, Satoshi  
Department of Mechanical Engineering, Kyushu University

Hirayama, Kyosuke  
Department of Mechanical Engineering, Kyushu University

Toda, Hiroyuki  
Department of Mechanical Engineering, Kyushu University

他

<https://hdl.handle.net/2324/4150459>

---

出版情報 : Materials Science and Engineering : A. 766, pp.138264-, 2019-10-24. Elsevier  
バージョン :  
権利関係 :



**Title:**

**Effects of 3D Microstructural Distribution on Short Crack Growth Behavior in two Bimodal Ti-6Al-4V Alloys**

**Authors:**

M. Hassanipour <sup>a</sup>, S. Watanabe <sup>a</sup>, K. Hirayama <sup>a</sup>, H. Toda <sup>a</sup>, K. Uesugi <sup>b</sup>, A. Takeuchi <sup>b</sup>

**Affiliations:**

<sup>a</sup> Department of Mechanical Engineering, Kyushu University, 744, Motooka, Nishi Ward, Fukuoka, Fukuoka 819-0395, Japan

<sup>b</sup> Japan Synchrotron Radiation Research Institute, 1-1-1, Kouto, Sayo Cho, Sayo Gun, Hyogo 679-5148, Japan

**Corresponding Author:**

M. Hassanipour

Email: hassanipourm@mech.kyushu-u.ac.jp

Phone: +81-92-802-3215

## Abstract

In situ X-ray micro-tomography was performed to analyze the short crack growth in the microstructure ( $\alpha$ ,  $\alpha+\beta$  phases and  $\alpha/\alpha+\beta$  interface) of two Ti-6Al-4V alloys. Short crack strongly interacts with the local microstructure and it grows into the predominant phase above the average microstructural fraction in each alloy. The increase in the volume fraction and size of the  $\alpha$  grains results in a crack growth with lower variations and larger deflection lengths inside the clustered  $\alpha$  grains. As the short crack grows, the larger plastic zones size in the high  $\alpha$ -fraction alloy leads to the formation of secondary cracks and bifurcations that decrease the crack driving forces. Moreover, the larger deflections left behind the crack front induce higher crack closure and lower the crack driving forces. As a result, the short crack in the high  $\alpha$ -phase fraction alloy remains sensitive to the local microstructural features at higher lengths.

**Key Words:** Short crack propagation, Xray micro-tomography, Bimodal, Ti-6Al-4V, Microstructure

## 1.Introduction

The bimodal Ti-6Al-4V alloys, which are widely used to manufacture compressor disks and blades of jet-engines, have the advantage to combine a good ductility and fatigue crack propagation resistance [1,2]. However, during the service load, small defects propagate with high crack growth rate variation due to the interaction with three dimensional (3D) microstructural features such as grain/phase shape, size, volume fraction in these alloys [3,4].

Previous studies have reported that a decrease in the average grain size ( $\alpha$  and  $\alpha+\beta$ ) causes a decrease in the average short crack growth rate, which leads to a better fatigue life in titanium alloys [5–7]. There is an agreement that a decrease in grain size leads to an increase in grain boundaries that are microstructural barriers impeding the crack growth [8,9]. However, as the short crack grows from the grain boundary to the next grain/phase, there may be a change in crack path (deflection) due to a change in microstructural features of the subsequent grain/phase [10,11]. These deflections are left in the crack wake creating a rough surface that results in a decrease in the crack driving forces and growth rate [12,13]. It has been shown that an increase in grain size leads to larger deflections with lower crack growth rates [14,15].

In alloys with high  $\alpha$ -phase volume fraction, cluster of  $\alpha$  grains favorably oriented for short crack growth on the basal plane leads to facet-like fracture path with high rates [16–18]. By decreasing the  $\alpha$ -phase fraction, there is a lower probability to have cluster of the aforementioned grains which may result in low crack growth rates and a better fatigue life [19–21]. Nevertheless, the short crack growth rate and its variation are controlled by the local distribution of various microstructural features around the crack path [22,23].

As the short crack length increases, there is an increase in crack tip plastic zones and its driving forces, so the crack becomes less sensitive to the variation of local features [24]. As a result, the crack has higher crack growth rate with lower variation and it is so-called long with respect to the microstructure [25]. It has been reported that the transition from short to long crack corresponds to a crack length that is 5 to 10 times

larger than a microstructural element, which is conventionally considered to be the mean grain size [26]. However, there is not a clear demarcation, since this transition depends on various microstructural features and loading conditions [27,28]. It can be said that the transition from short to long crack is affected by the local microstructural features interacting with the growing crack.

In this study, the crack propagation in the microstructure ( $\alpha$ ,  $\alpha+\beta$  phases, and interface) at sub-grain level growth (5  $\mu\text{m}$ ) is investigated at increasing number of fatigue cycles in low and high  $\alpha$ -phase volume fraction Ti-6Al-4V alloys. Moreover, the short crack length is analyzed at two different lengths in order to estimate the change in the interaction between the 3D crack and microstructure. This transitional interaction and its effect on the 3D crack growth rate variations are studied in both alloys.

## 2. Material and experimental procedures

In this study, heat treatment was performed on two Ti-6Al-4V alloys. The first alloy was solution heat treated at 940°C for 2 hours followed by water quenching; afterwards, it was tempered at 705°C for 2 hours followed by air cooling. The second alloy was hot rolled at 800°C resulting in a 50% overall thickness reduction. Afterwards, it was tempered up to 900°C during 96 hours in the furnace and cooled down to the room temperature.

At the end of heat treatment, the first alloy was composed of 40% hexagonal close-packed (hcp) primary  $\alpha$  phase and 60% of  $\alpha+\beta$  phase consisting of acicular secondary  $\alpha$  phase within the body center cubic (bcc)  $\beta$  phase. The volume fractions of phases in the second alloy were 65% and 35%, respectively. The first and second bimodal alloys will be called hereafter microstructure B1 and B2, respectively. The average grain size of  $\alpha$  grains in both alloys were measured by using the electron backscattering analysis (EBSD). The average grain size was equal to 13 and 23  $\mu\text{m}$  in microstructure B1 and B2, respectively. The L, T, and S in Figure 1 correspond to longitudinal, transverse and short transverse directions, respectively in the low  $\alpha$ -fraction alloy. The ND, TD, and RD correspond to normal, transverse and rolling directions, respectively in the high  $\alpha$ -fraction alloy. In the following sections L, T, and S followed by ND, TD, and RD are referred as x, y, z.

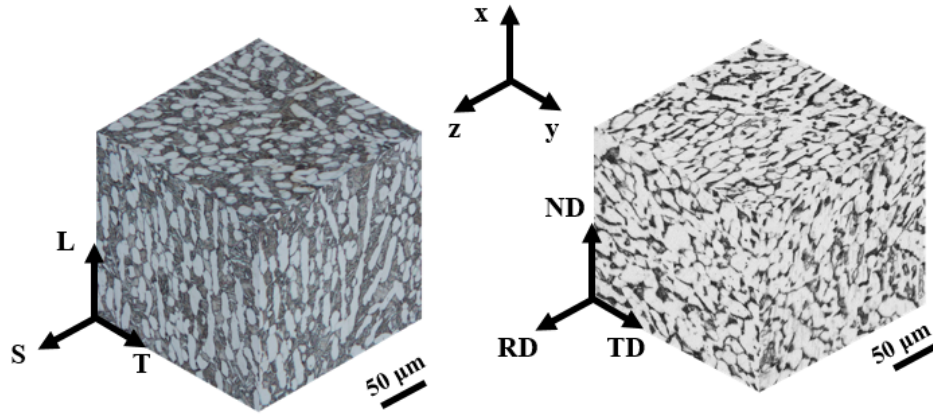


Figure 1. Revealed microstructure of the two bimodal Ti-6Al-4V, a) microstructure B1 and, b) macrostructure B2.

Tensile test showed that yield stresses were equal to 996 and 814 MPa, respectively, in the low and high  $\alpha$ -fraction alloys. The ultimate tensile strengths were equal to 1158 and 934 MPa, respectively. Fatigue tests were performed at  $R = 0.1$  with a frequency of 15 Hz on specimens with a square cross section of  $600 \times 600 \mu\text{m}$  for both alloys. Load directions was along the  $z$  axis for both microstructures. In order to be able to follow a main crack in the specimen, a notch with dimensions of  $60 \times 20 \times 4 \mu\text{m}$  ( $x, y, z$ , respectively) was made prior to the fatigue tests on the surface of the specimens using a focused ion beam. The preliminary fatigue test showed that a maximum stress of 778 MPa results in average fatigue life of 26000 and 30000 cycles in specimens with the low and high  $\alpha$ -fraction alloys, respectively. Those fatigue lives correspond to the low cycle fatigue regime for both specimens. As a result, the fatigue tests were conducted with the aforementioned load conditions.

While in situ computed tomography (CT) at the BL20XU beamline of SPring-8 was employed to scan the growing crack inside the alloy. The monochromatic X-ray energy of 30keV was produced by a liquid nitrogen-cooled Si (111) double crystal monochromator. A CMOS camera was used for acquiring the projection images.

The sample distance to source were 80 and 240 m for the high and low  $\alpha$ -fraction alloys, respectively. The specimens distance from the camera were set to 53, 150, and 250 mm in order to obtain phase contrast images that render the highest contrast between the  $\alpha$  and  $\alpha+\beta$  phases [29]. The distances equal to 53 and 150 mm rendered the best contrast between phases for the high and low  $\alpha$ -fraction alloys, respectively. During 180 degrees of stage rotation with 0.1 degree step, 1800 scans were conducted with an exposure time of 400 ms and the voxel size was equal to  $0.5 \mu\text{m}$ , details can be found in [27]. The crack was periodically scanned for every  $5 \mu\text{m}$  of crack growth projection on the detector. This scanning was performed from 107 to 159  $\mu\text{m}$  and from 105 to 156  $\mu\text{m}$  (first region) for the low and high  $\alpha$ -fraction alloys, respectively. For a larger crack front in a second region, the crack was scanned from 300 to 354  $\mu\text{m}$  and from 292 to 342  $\mu\text{m}$ , respectively. The scanning in two regions enabled us to investigate the transitional behavior from short to long crack for both alloy within similar ranges.

Gray value thresholding combined with the seed growth technique [30] were employed for all cycles in order to extract the 3D crack using the absorption images (Figures 2(a)) [27]. The crack growth rates were calculated by using the coordinates of two subsequent cycles. The applied procedure led to 5% of negative crack growth rate for each two subsequent cycles.

The absorption images were converted to phase contrast images using a phase retrieval technique [31], which led to an increase in the difference between the average gray values of  $\alpha$  and  $\alpha+\beta$  phases (Figure 2(b)). By defining a threshold between the average gray values of  $\alpha$  and  $\beta$ , the phase contrast slice images were binarized (Figures 2 (c)), so  $\alpha$  and  $\alpha+\beta$  phase were defined by white and black voxels, respectively.

The crack tip was identified in the absorption slice image (Figures 2 (d)). Afterwards, a region of  $1.5 \times 1.5 \times 1.5 \mu\text{m}$  (twenty seven voxels) was defined around the crack tip in order to determine its location in the microstructure (Figures 2(e) and (f)). A location with twenty seven white voxels shows that the crack tip is in the  $\alpha$  phase and a location with twenty seven black voxels indicates that the crack tip is in the  $\alpha+\beta$  phase. An intermediate value implies that the crack tip is located in the interface.

The average crack front fraction in the microstructure was calculated by averaging the crack tip locations in the  $\alpha$ ,  $\alpha+\beta$ , and interface for 5 semi-elliptical crack front inside both alloys. A homogeneous semi-elliptical crack implies that crack growth has no interaction with the microstructure and it grows in the  $\alpha$ ,  $\alpha+\beta$ , and interface with respect to the average microstructural fraction. At different crack lengths, crack front fraction in the microstructure was compared to the average microstructural fraction in order to evaluate the amount of crack front interaction with the microstructure. This procedure was employed to estimate the transition from short to long cracks in both alloys.

The cracked specimens were polished by serial sectioning in order to conduct the EBSD analysis around the crack path. The specimens were embedded in a resin and polished using 1200 and 4000 grit silicon carbide paper. Four microindentation were made in the specimen in order to ensure the uniform removal of the surface. This procedure was repeated until the crack section is  $30 \mu\text{m}$  away from the notch. Then, the surface was further polished with diamond and silica particles down to  $50 \text{ nm}$  for 3 hours. In order to investigate the effect crystallographic orientation of the grains on the short crack, the EBSD analysis was carried out around the crack path with  $0.2 \mu\text{m}$  step size. Afterwards, the crack surfaces were etched with a reagent consisting of 70%  $\text{H}_2\text{O}$ , 20%  $\text{HF}$ , and 10%  $\text{HNO}_3$  in order to reveal the microstructure.

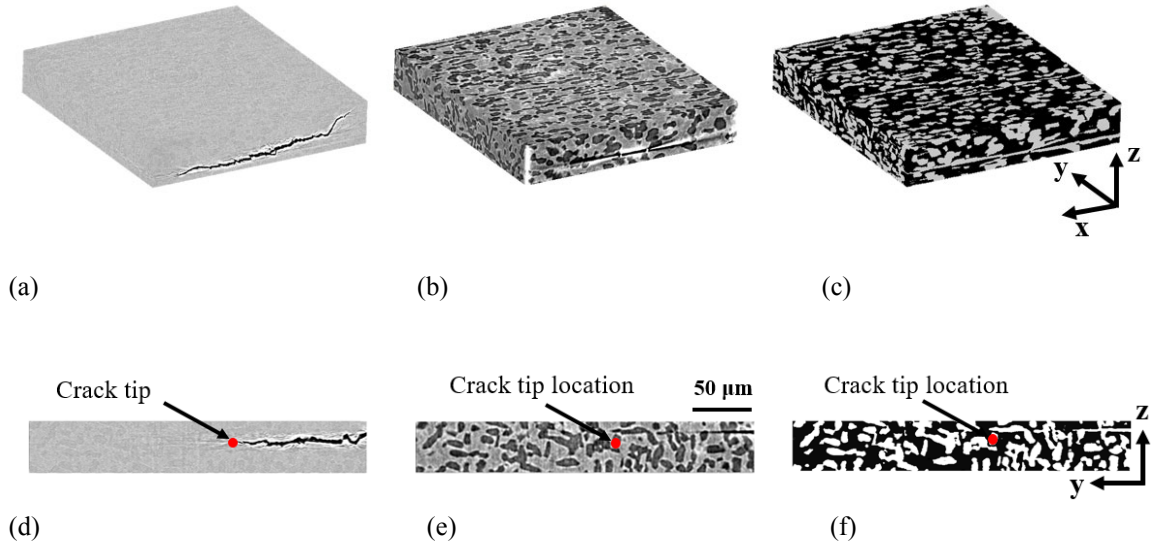


Figure 2. Procedure in order to determine the crack tip in the microstructure ( $\alpha$ ,  $\alpha+\beta$  phases and  $\alpha/\alpha+\beta$  interface). (a) Three dimensional rendering of crack and microstructure via absorption images, (b) view of 3D microstructure by using phase contrast images with its binarized version in (c). (d) Cross sectional slice image of (a) to determine crack tip and its corresponding location in the microstructure in (e) and (f).

### 3. Results

#### 3.1 Crack morphology

The three dimensional crack front projection images on xy, xz, and yz planes for microstructures B1 and B2 are shown in Figures 3. Within each region, there is a total of 10 interrupted cycles (crack front lines in Figures 3(a) and (b)) which results in 50  $\mu\text{m}$  crack front growth projection on the detector (xz planes). However, it required 5000 cycles in the microstructure B1 to reach 50  $\mu\text{m}$  as compared to 1900 cycles in the microstructure B2. As it can be seen from Figure 3(a), this is due to the larger crack growth inside the microstructure B1 as compared to the microstructure B2. This may be due to a variation in the plastic zone size along the crack front in the microstructure as reported [32].

In order to estimate the plastic zone variation along the crack front it is assumed that small scale yielding prevails. The crack dimensions, such as crack length on the surface (2c) and crack depth (a), are estimated for a semi-elliptical crack front in a similar approach to [34,35]. By using those dimensions, the stress intensity factor along the crack front is estimated by using the equation for semi-elliptical cracks reported in [33]. Afterwards, the plastic zone can be estimated by the following equation:

$$R_p = 1/T \times (K_{\max}/S_m)^2,$$

where  $R_p$  is the monotonic plastic zone size, T is a constant that depends on stress state along the crack front,  $K_{\max}$  is the maximum stress intensity and the  $S_m$  is the average sum of the yield stress and ultimate tensile strength. The estimated plastic zone sizes on the surface of the microstructure B1 is 29  $\mu\text{m}$ ; however,

this value decreases to 16.9  $\mu\text{m}$  in the center of crack front at point A1 in Figure 3(a). On the other hand, in the microstructure B2, the estimated plastic zone slightly decreases from 23.1  $\mu\text{m}$  on the surface to 21.9  $\mu\text{m}$  at the center of crack front at point A2 in Figure 3(b). As a result, the smaller plastic zone size inside the microstructure B1 induces a higher triaxial stress state and tensile stress inside the microstructure. This may lead to higher crack opening and crack growth rate inside the quasi-straight crack in the microstructure B1.

As the short crack front becomes larger to reach the beginning of the second region, 10 interrupted cycles results in 50  $\mu\text{m}$  crack front growth. This crack growth required 940 cycles in the microstructure B1 as compared to the 1560 cycles in the microstructure B2. By comparing the number of elapsed cycles for similar crack growth in the first and second regions in the microstructure B1 (5000 cycles versus 940 cycles), it can be said that there is a high increase in crack growth rates. On the other hand, there is only a slight increase in the crack growth rates in the microstructure B2.

The short crack fronts in both alloys have an inhomogeneous shape at the beginning of the first region. However, at the end of the first region, the crack front in the microstructure B1 reaches a quasi-homogenous shape as opposed to the crack front in the microstructure B2. This implies that the crack front has still a strong interaction with the microstructure in the microstructure B2.

As the short crack becomes larger in the second region, the crack in the microstructure B1 remains quasi-homogeneous, but the crack in the microstructure B2 still interacts with the microstructure at some locations. The short crack consists of quasi-straight paths in the microstructure B1 (Figures 3(c) and (e)) as compared to crack complex paths with bifurcations and secondary cracks (Figures 3(d) and (f)) in the microstructure B2.



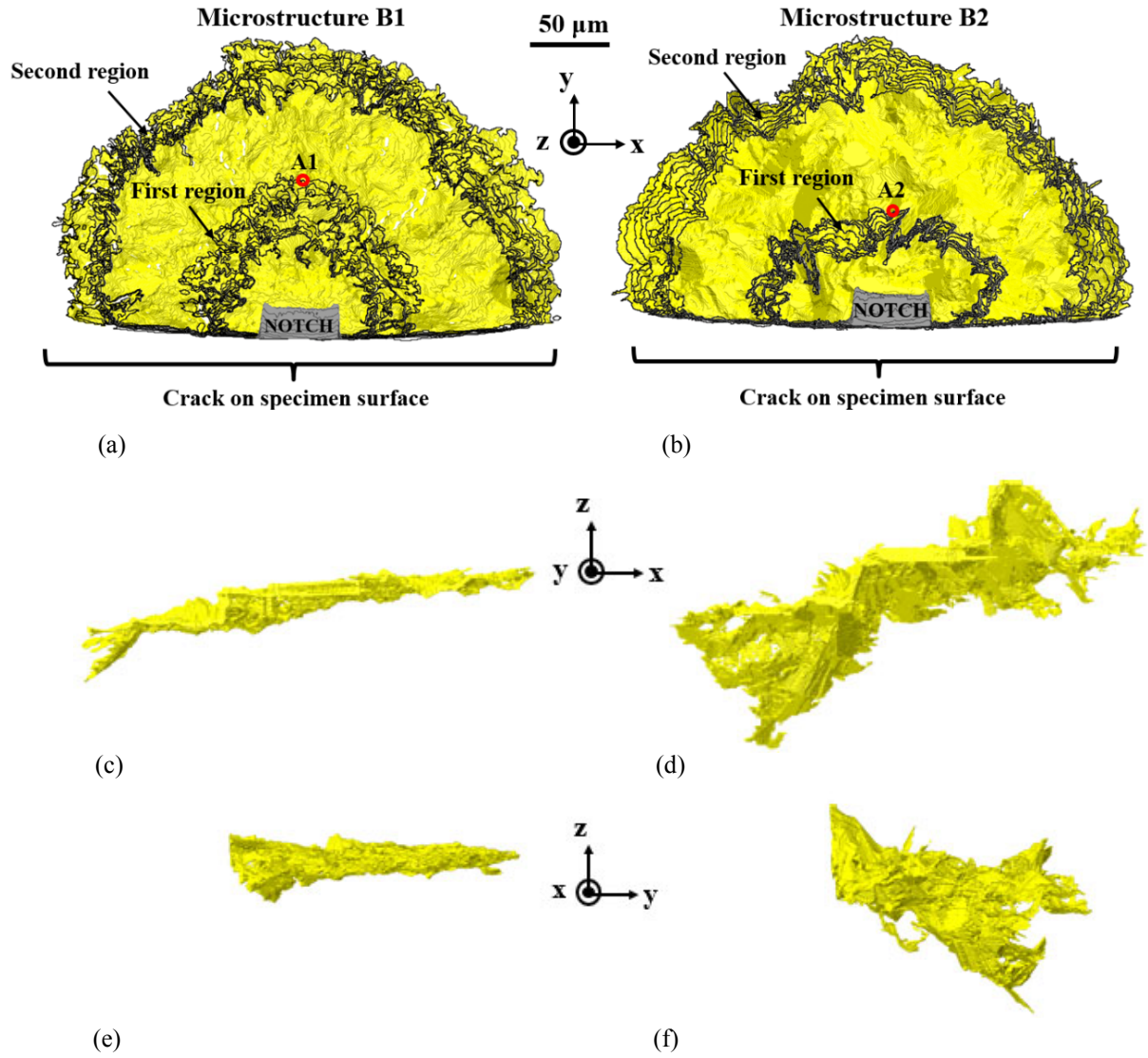


Figure 3. Three dimensional crack projection images on xy plane with each line corresponding to an interrupted load cycle in the the first and second regions for (a) microstructure B1 and, (b) B2 [27]. Crack front projection on xz and yz planes, respectively, in (c) and (e) for the microstructure B1 followed by (d) and (f) for the microstructure B2.

### 3.2 Quantification of short crack growth rate on the surface and in the bulk

The average short crack growth rates on the surface and inside both microstructures are compared in Figures 4. It can be seen that the short crack growth rates on the surface have higher variation as compared in the bulk (inside the alloys) for both regions. This may be due to the three dimensional constraint imposed by the surrounding grains to the cracked grains in the bulk. In the first region, the crack growth rates in the bulk are higher than those on the surface in the microstructure B1 (Figure 4(a)), while they are by average

similar in the microstructure B2 (Figure 4(b)). As the short crack becomes larger in the second region, the crack growth rate in the bulk becomes gradually much higher for the microstructure B1 as compared to the microstructure B2. However, the average short crack growth rates on the surface are similar in both microstructures.

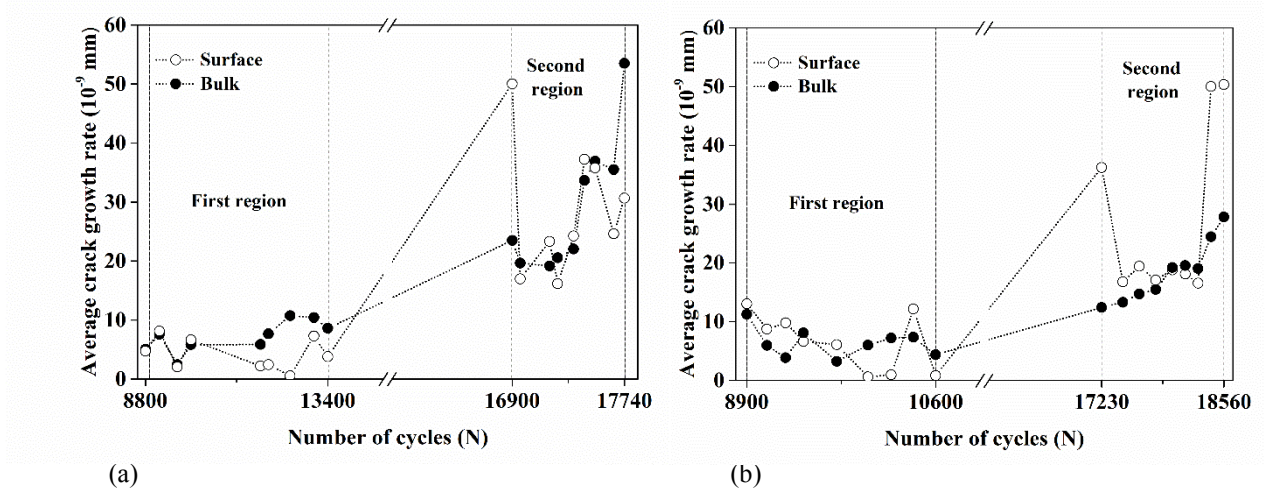


Figure 4. Comparison of average crack growth rate on the surface and in the bulk for the (a) microstructure B1, and (b) microstructure B2.

The spatial crack growth rate in the  $\alpha$ ,  $\alpha+\beta$  phases, and interface ( $\alpha$ ,  $\alpha+\beta$ ) along the crack front line in both microstructures are shown in Figures 5. The crack growth rates for both microstructures were normalized with the maximum crack growth rates in the first and second regions corresponding to 78.3 and 261, respectively. The crack growth rates in the microstructure are shown with respect to the distance along the crack front line, which is the sum of crack segments along the crack front from the right the side of the notch until the left side on the surface.

Short crack growth rate has high variation along the crack front in both microstructures as shown in Figures 5. The short crack is growing with higher rates and variations in the microstructure B1 as compared to B2 (Figure 5(a) versus Figure 5(b)). Crack paths in both alloys consist of facet-like paths (mainly induced in  $\alpha$  phase) and zigzag paths (mainly induced in  $\alpha+\beta$  phase).

As the short crack grows into the second region, there is a high increase in crack growth rates in the  $\alpha$ ,  $\alpha+\beta$  phases, and interface in the microstructure B1 (Figure 5(c) versus Figure 5(a), considering the normalized values). On the other hand, there is a slight increase in short crack growth rates in the microstructure B2 (Figure 5(d) versus Figure 5(b)). Nonetheless, crack growth rates increase in  $\alpha$  phase at some locations along the crack front line.

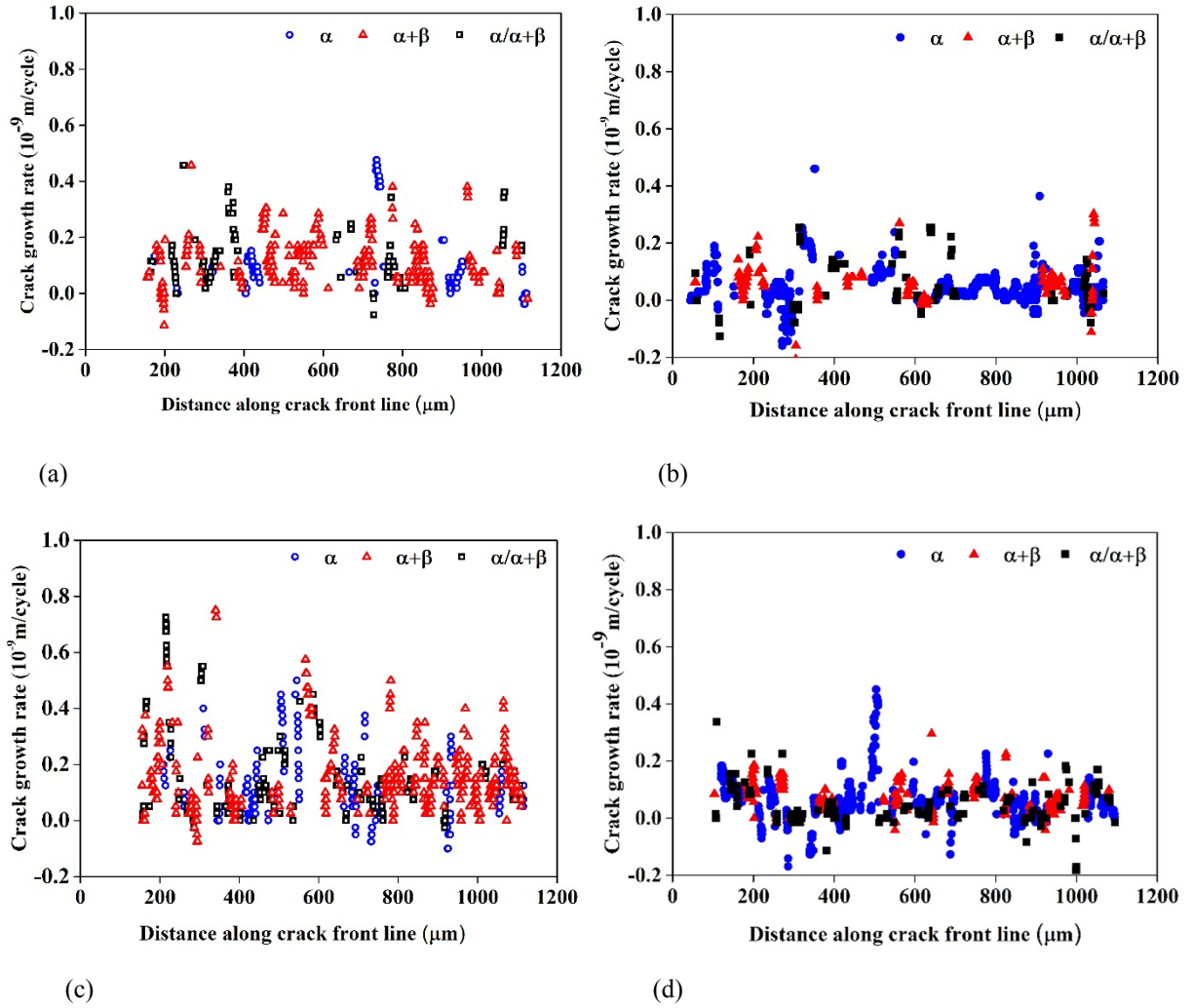


Figure 5. Spatial crack growth rate variation in the microstructure ( $\alpha$ ,  $\alpha+\beta$  phases and  $\alpha/\alpha+\beta$  interface) at a representative load cycle in the first region for (a) microstructure B1, and (b) microstructure B2 followed by a load cycle in the second region for (c) microstructure B1, and (d) microstructure B2. Crack growth rates were normalized with 78.3 and 261, which are the maximum crack growth rates in the first and second regions, respectively.

## 4. Discussion

### 4.1 Short crack path analysis

It is presumed that a homogenous semi-elliptical crack front grows without any microstructural preference with an average fractional value in each phase. The crack front interaction with the microstructure induces an inhomogeneous crack growth which is compared to the average fraction. Figures 6 show the crack front percentage in  $\alpha$ ,  $\alpha+\beta$  phases, and interface for each load cycle in two crack front regions.

It can be inferred from Figures 6(a) that the crack prefers to grow above the average microstructural fraction in  $\alpha+\beta$  phase in the microstructure B1. As the  $\alpha$  phase fraction and the average  $\alpha$  grain size increase, short crack grows in the predominant  $\alpha$  phase above the average microstructural fraction (Figure 6(b)). This shows that the crack prefers to grow inside the predominant phase in both microstructures rather growing in the other phase and interface. The high variation in crack growth in microstructure B1 induces higher variation in the interface as opposed to microstructure B2 (Figure 6(c)). At the end of first region, where the average crack length is 10 times larger than the average grain size in the microstructure B1, short crack grows towards the average microstructural fraction (especially in the predominant  $\alpha+\beta$  phase), so it becomes less sensitive to the microstructure. On the other hand, in the microstructure B2 with a crack length that is 4.3 times larger than the grain size, the short crack grows above the average fraction in  $\alpha$  phase, so it maintains the interaction with the microstructure.

As the short crack front becomes larger in the second region (within 300 to 330  $\mu\text{m}$ ), it grows in  $\alpha$  and  $\alpha+\beta$  phases close to the average microstructural fraction in the microstructure B1, which ensures that crack is less sensitive to the microstructure. On the other hand, in the microstructure B2, crack front in  $\alpha$  and  $\alpha+\beta$  phases is below and above the average microstructural fractions, respectively. Thus, as the average crack length grows from 13 to 14.3 times larger than the average grain size, the crack is still sensitive to the microstructure. The crack front percentages in interface are above the average microstructural fraction in both alloys in the second region.

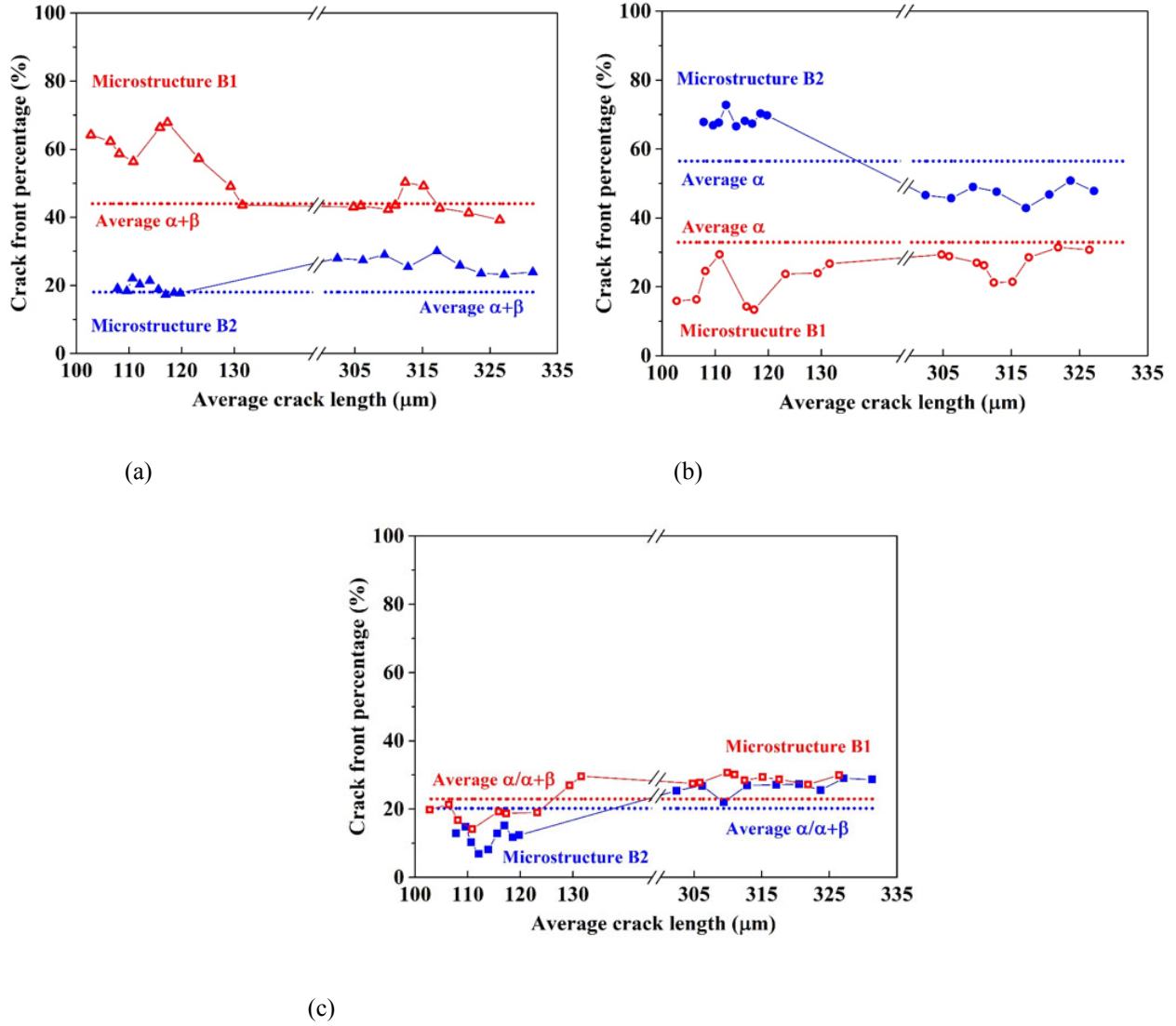


Figure 6. Average crack front percentage in (a)  $\alpha+\beta$ , and (b)  $\alpha$  phases and (c) interface with respect to the average crack length in microstructures B1 and B2.

Short crack growth inside the  $\alpha$  and  $\alpha+\beta$  phases in the microstructure B1 has higher variations as compared to the quasi-stable growth in the microstructure B2. As the short crack enters the grain/phase, it may deflect by an angle in order to follow the planes with the highest shear stress until it reaches the next grain/phase. Crack grows in  $\alpha+\beta$  grains through successive  $\alpha$  and  $\beta$  laths, with different crystallographic orientations that is of an order of 1 μm, with short deflection lengths. Regarding the crack growth in  $\alpha$  grains, cracking mainly occurs in facet-like paths on the basal plane.

Short crack path in the microstructure B1 with predominant  $\alpha+\beta$  phase and smaller  $\alpha$  grains has higher variation in crystallographic orientations along the crack path that can be seen in Figure 7(a). This induces short deflections length that results in a quasi-planar crack surface. On the other hand, crack grows in continuous facet-like paths (large deflection lengths) that can be an average order of  $\alpha$  grain size that is 23 μm (see Figure 7(b)) in the microstructure B2 with predominant fraction of  $\alpha$  grains. As a result for the



same crack distance there is a lower variation in the crystallographic orientations in the microstructure that may cause the stable growth in the microstructure B2.

As the short crack length increases in the second region, the plasticity and crack driving forces at the crack tip gradually increase in both alloys. The estimated plastic zones in the center of the crack front are 32.6 and 49.6  $\mu\text{m}$  in the microstructure B1 and B2, respectively. Thus, the larger plastic zone in the microstructure B2 leads to the formation of secondary cracks and bifurcations which cause a decrease in crack driving forces (Figure 7(b)). Moreover, the higher surface roughness can lead to premature crack contacts in the microstructure B2. These mechanisms induce a decrease in crack front driving forces so the short crack remains sensitive to the microstructure at higher lengths.

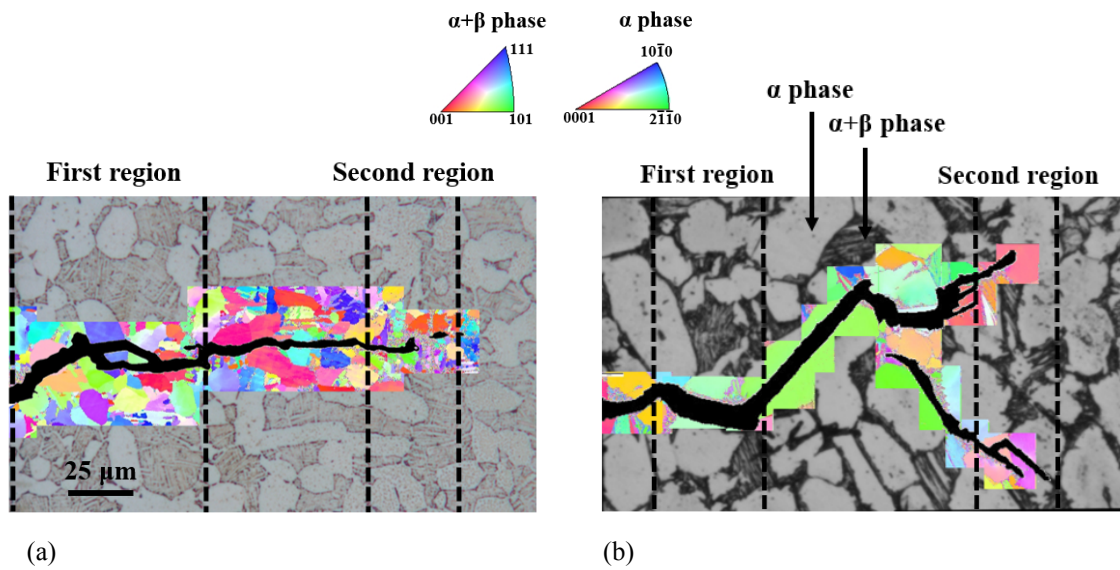


Figure 7. Schematic of short crack path in both microstructures. (a) Short crack with short deflection lengths in microstructure B1, as opposed to (b) with large deflection lengths in the microstructure B2.

#### 4.2 Short crack growth rate in the phases and interface

The average crack growth rate in the microstructure for both microstructures are shown in Figures 8. The short crack growth rates in  $\alpha$  phase are similar for both microstructures at lower crack length in the first region. It can be said that an increase in the fraction and size of the  $\alpha$  grains may cause a lower crack growth rate variation in the microstructure B2 in but it does not lead to higher crack growth rate (Figure 8(a)). This lower variation may be due to the crack growth inside the larger  $\alpha$  grains as compared to the microstructure B1. On the other hand, short crack growth rate in the  $\alpha+\beta$  phase have similar variations in both alloys but there is a gradual increase in the crack growth rate in the microstructure B1 (Figure 8(b)). At the end of the first region (from 120  $\mu\text{m}$  to 130  $\mu\text{m}$ ), there is a decrease in crack growth rate variation in the microstructure B1, which implies that the effect of local microstructural features are decaying in this alloy.

In the second region, the short deflection lengths left in the crack path induces a lower roughness in the

microstructure B1. It is reported that a low crack roughness leads to a low crack closure level which causes a high crack growth rate [12,36]. As a result, the lower crack roughness in the microstructure B1 leads to higher crack growth rates in  $\alpha$ ,  $\alpha+\beta$  phases, and interface as compared to the microstructure B2.

The short crack growth rate in the interface has the highest variation in both microstructures (Figure 8(c)). This may be due to the variation across the boundaries between  $\alpha$  and  $\alpha+\beta$  phase in both microstructures. At higher crack length, those variations gradually decrease.

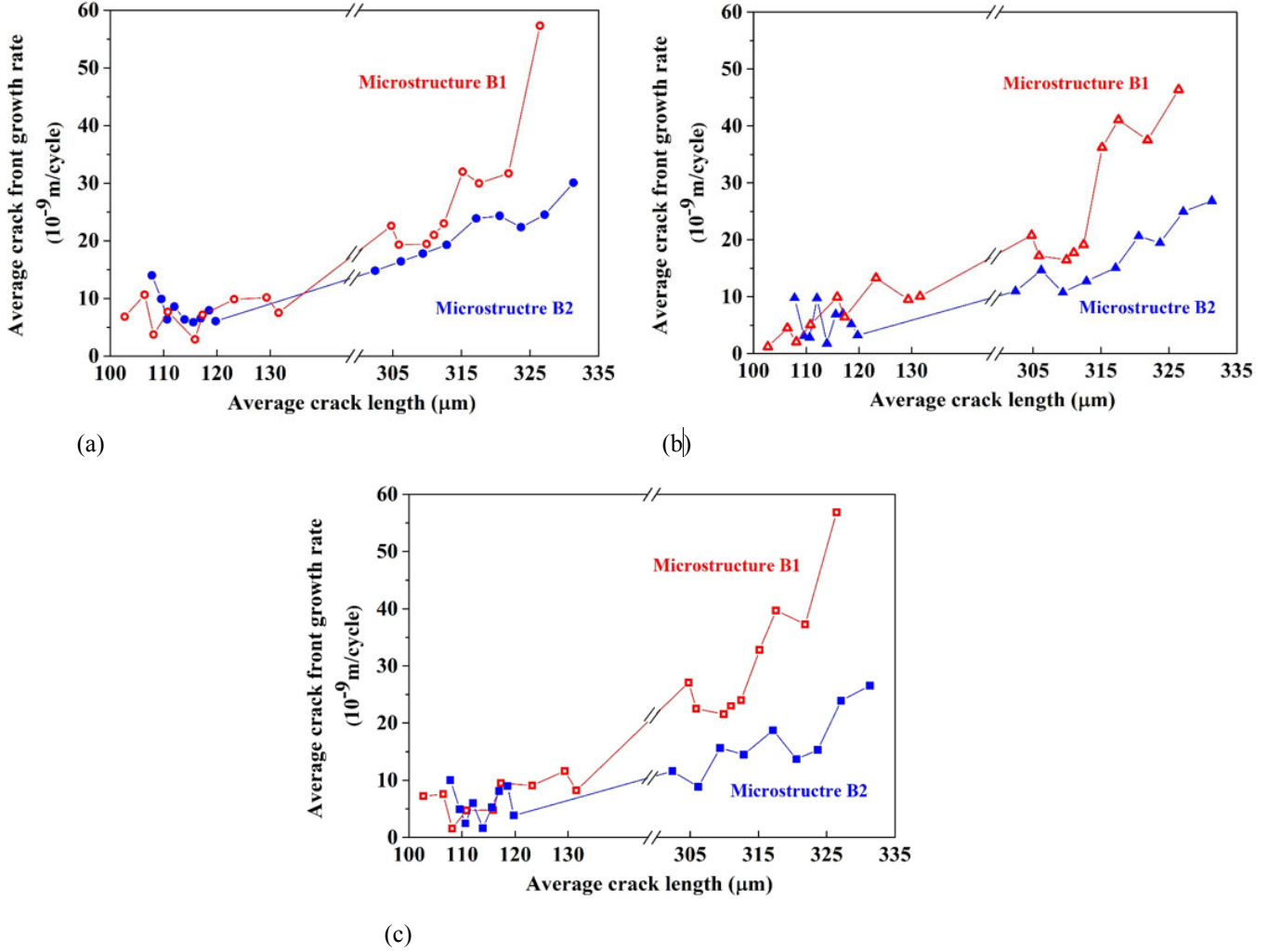


Figure 8. Average crack growth rate with respect to the average crack length in (a)  $\alpha$ , (b)  $\alpha+\beta$  phases, and (c) interface for the microstructure B1 and B2.

## 4. Conclusions

In summary, in situ computed X-ray microtomography was performed during a low cycle fatigue test to quantify crack growth behavior at every 5  $\mu\text{m}$  in two bimodal Ti-6Al-4V microstructure (i.e.  $\alpha$ ,  $\alpha+\beta$  phases and interface). The combination of X-ray microtomography with the phase retrieval technique aids to enhance the contrast between the  $\alpha$  and  $\alpha+\beta$  phases in the microstructure. By using the aforementioned

method, the crack front percentage and crack growth rate were quantified inside each phase and along the interface. The comparison between the crack front fraction inside the microstructure as compared to the average microstructural fraction were used to estimate the amount of crack interaction with the microstructure. The two bimodal Ti-6Al-4V with predominant  $\alpha+\beta$  and  $\alpha$  phase volume fraction were referred to as microstructure B1 and B2.

The short crack growth rate has higher variation on the surface than in the bulk for both microstructures. This may be due to the three dimensional constraint imposed by the surrounding grains in the bulk as compared to the surface. In the microstructure B1, crack grows with higher rates inside the microstructure as compared to the surface that may be due to the higher stress triaxiality inside this microstructure.

Short crack grows inside the predominant phase above the average microstructural fraction in each microstructure. The short crack has lower variations in growth and in growth rate inside the microstructure B2. This may due to the higher fraction of  $\alpha$  phase with larger  $\alpha$  grains size that results in lower variation in crystallographic orientation of grains in the microstructure B1.

As the short crack becomes larger, it grows close to the average microstructural fraction in the microstructure B1, but it is still below the average fraction and it remains sensitive to the microstructure in the microstructure B2. The larger plastic zones size in the microstructure B2 alloy leads to the formation of secondary cracks and bifurcations that decrease the crack tip driving forces. Moreover, the higher surface roughness left behind the crack front induces a higher crack closure level leading to a reduction in crack tip driving forces. As a result, the short crack remains sensitive to the microstructure at higher crack lengths and larger crack fronts. In addition, the decrease in crack tip driving forces leads to lower crack growth rates in  $\alpha$ ,  $\alpha+\beta$  phases and interface in the microstructure B2.

## Acknowledgments

The synchrotron radiation experiments were performed at SPring-8 with the approval of Japan Synchrotron Radiation Research Institute (JASRI) through proposal numbers of 2016B0076, 2017A0076 and, 2017B0076. This work was supported through the grant-in-aid for scientific research from Structural Materials for Innovation (SM4I) of the Cross-ministerial Strategic Innovation Promotion Program (SIP). The authors gratefully acknowledge the support of Light Metal Educational Foundation (LMEF).

## References

- [1] D. Banerjee, J.C. Williams, Perspectives on titanium science and technology, *Acta Mater.* 61 (2013) 844–879.
- [2] N. Verdhhan, D.D. Bhende, R. Kapoor, J.K. Chakravartty, Effect of microstructure on the fatigue crack growth behaviour of a near- $\alpha$  Ti alloy, *Int. J. Fatigue.* 74 (2015) 46–54.



- doi:10.1016/j.ijfatigue.2014.12.013.
- [3] J.R. Mayeur, D.L. McDowell, A three-dimensional crystal plasticity model for duplex Ti-6Al-4V, *Int. J. Plast.* 23 (2007) 1457–1485. doi:10.1016/j.ijplas.2006.11.006.
  - [4] S. Jadhav, A. Powar, S. Patil, A. Supare, B. Farane, R. Singh, Effect of volume fraction of  $\alpha$  and transformed  $\beta$  on the high cycle fatigue properties of bimodal Ti6Al4V alloy, *IOP Conf. Ser. Mater. Sci. Eng.* 201 (2017). doi:10.1088/1757-899X/201/1/012035.
  - [5] C.P. Przybyla, D.L. McDowell, Microstructure-sensitive extreme-value probabilities of high-cycle fatigue for surface vs. subsurface crack formation in duplex Ti-6Al-4V, *Acta Mater.* 60 (2012) 293–305. doi:10.1016/j.actamat.2011.09.031.
  - [6] G. Lütjering, Influence of processing on microstructure and mechanical properties of ( $\alpha$ + $\beta$ ) titanium alloys, *Mater. Sci. Eng. A.* 243 (1998) 32–45. doi:10.1016/S0921-5093(97)00778-8.
  - [7] K. Tokaji, T. Ogawa, K. Ohya, The effect of grain size on small fatigue crack growth in pure titanium, *Int. J. Fatigue.* 16 (1994) 571–578. doi:10.1016/0142-1123(94)90483-9.
  - [8] A. Navarro, E.R. Rios, A microstructurally short fatigue crack growth equation, *Fatigue Fract. Eng. Mater. Struct.* 11 (1988) 383–396.
  - [9] A. Navarro, E.R. d. L. Rios, a Model for Short Fatigue Crack Propagation With an Interpretation of the Short–Long Crack Transition, *Fatigue Fract. Eng. Mater. Struct.* 10 (1987) 169–186. doi:10.1111/j.1460-2695.1987.tb01158.x.
  - [10] T. Zhai, A.J. Wilkinson, J.W. Martin, A crystallographic mechanism for fatigue crack propagation through grain boundaries.pdf, 48 (2000) 4917–4927.
  - [11] T. Zhai, X.P. Jiang, J.X. Li, M.D. Garratt, G.H. Bray, The grain boundary geometry for optimum resistance to growth of short fatigue cracks in high strength Al-alloys, *Int. J. Fatigue.* 27 (2005) 1202–1209. doi:10.1016/j.ijfatigue.2005.06.021.
  - [12] R.K. Nalla, J.P. Campbell, R.O. Ritchie, Mixed-mode, high-cycle fatigue-crack growth thresholds in Ti-6Al-4V: Role of small cracks, *Int. J. Fatigue.* 24 (2002) 1047–1062. doi:10.1016/S0142-1123(02)00020-8.
  - [13] S. Suresh, R.O. Ritchie, Propagation of short fatigue cracks, *Int. Met. Rev.* 29 (1984) 445–475. doi:10.1179/imtr.1984.29.1.445.
  - [14] Y.Q. Chen, S.P. Pan, M.Z. Zhou, D.Q. Yi, D.Z. Xu, Y.F. Xu, Effects of inclusions, grain boundaries and grain orientations on the fatigue crack initiation and propagation behavior of 2524-T3 Al alloy, *Mater. Sci. Eng. A.* 580 (2013) 150–158. doi:10.1016/j.msea.2013.05.053.
  - [15] T. Hanlon, E.D. Tabachnikova, S. Suresh, Fatigue behavior of nanocrystalline metals and alloys, *Int. J. Fatigue.* 27 (2005) 1147–1158. doi:10.1016/j.ijfatigue.2005.06.035.
  - [16] F. Bridier, P. Villechaise, J. Mendez, Slip and fatigue crack formation processes in an  $\alpha/\beta$  titanium alloy in relation to crystallographic texture on different scales, *Acta Mater.* 56 (2008) 3951–3962.

- [17] I. Bantounas, T.C. Lindley, D. Rugg, D. Dye, Effect of microtexture on fatigue cracking in Ti–6Al–4V, *Acta Mater.* 55 (2007) 5655–5665.
- [18] V. Sinha, M.J. Mills, J.C. Williams, J.E. Spowart, Observations on the faceted initiation site in the dwell-fatigue tested Ti-6242 alloy: crystallographic orientation and size effects, *Metall. Mater. Trans. A.* 37 (2006) 1507–1518.
- [19] D.L. McDowell, F.P.E. Dunne, Microstructure-sensitive computational modeling of fatigue crack formation, *Int. J. Fatigue.* 32 (2010) 1521–1542. doi:10.1016/j.ijfatigue.2010.01.003.
- [20] C.P. Przybyla, *Microstructure-Sensitive Extreme Value Probabilities of Fatigue in Advanced Engineering Alloys*, 2010.
- [21] S. Ivanova, R.R. Biederman, R.D.S. Jr, Investigation of Fatigue Crack Initiation in Ti-6Al-4V During Tensile-Tensile Fatigue Investigation of Fatigue Crack Initiation in Ti-6Al-4V During Tensile-Tensile Fatigue, *J. Mater. Eng. Perform.* 11 (2002) 226–231.
- [22] A.L. Dowson, A.C. Hollis, C.J. Beevers, The effect of the alpha-phase volume fraction and stress ratio on the fatigue crack growth characteristics of the near-alpha IMI 834 Ti alloy, *Int. J. Fatigue.* 14 (1992) 261–270. doi:10.1016/0142-1123(92)90010-A.
- [23] C.W. Brown, D. Taylor, The effects of texture and grain size on the short fatigue crack growth rate in Ti-6Al-4V, in: *Fatigue Crack Growth Threshold Concepts*, 1984: pp. 433–446.
- [24] M. Hassanipour, S. Watanabe, K. Hirayama, H. Li, H. Toda, K. Uesugi, A. Takeuchi, Coarsening of Complex 3D Microstructure and Short Crack Growth Correlation by a Surrogate Model in Ti-6Al-4V, To Be Submitted to *Acta Mater.* (n.d.) 1–17.
- [25] K. Tokaji, T. Ogawa, S. Osako, the Growth of Microstructurally Small Fatigue Cracks in a Ferritic–Pearlitic Steel, *Fatigue Fract. Eng. Mater. Struct.* 11 (1988) 331–342. doi:10.1111/j.1460-2695.1988.tb01387.x.
- [26] J. Lankford, the Influence of Microstructure on the Growth of Small Fatigue Cracks, *Fatigue Fract. Eng. Mater. Struct.* 8 (1985) 161–175. doi:10.1111/j.1460-2695.1985.tb01201.x.
- [27] M. Hassanipour, S. Watanabe, K. Hirayama, H. Toda, K. Uesugi, A. Takeuchi, Short Crack Growth Behavior and its Transitional Interaction with 3D Microstructure in Ti-6Al-4V, *Mater. Sci. Eng. A.* 738 (2018) 229–237. doi:10.1016/j.msea.2018.09.073.
- [28] B. Künkler, O. Düber, P. Köster, U. Krupp, C.P. Fritzen, H.J. Christ, Modelling of short crack propagation - Transition from stage I to stage II, *Eng. Fract. Mech.* 75 (2008) 715–725. doi:10.1016/j.engfracmech.2007.02.018.
- [29] H. Toda, A. Takijiri, M. Azuma, S. Yabu, K. Hayashi, D. Seo, M. Kobayashi, K. Hirayama, A. Takeuchi, K. Uesugi, Damage micromechanisms in dual-phase steel investigated with combined phase- and absorption-contrast tomography, *Acta Mater.* 126 (2017) 401–412.
- [30] H. Toda, I. Sinclair, J.Y. Buffière, E. Maire, T. Connolley, M. Joyce, K.H. Khor, P. Gregson, Assessment of the fatigue crack closure phenomenon in damage-tolerant aluminium alloy by in-

- situ high-resolution synchrotron X-ray microtomography, *Philos. Mag.* 83 (2003) 2429–2448. doi:10.1080/1478643031000115754.
- [31] D. Paganin, S.C. Mayo, T.E. Gureyev, P.R. Miller, S.W. Wilkins, Simultaneous phase and amplitude extraction from a single defocused image of a homogeneous object, *J. Microsc.* 206 (2002) 33–40. doi:10.1046/j.1365-2818.2002.01010.x.
  - [32] J. Schijve, The effect of pre-strain on fatigue crack growth and crack closure, *Eng. Fract. Mech.* 8 (1976) 575–581. doi:10.1016/0013-7944(76)90031-X.
  - [33] I.R. JC Newman, Stress-intensity factor equations for cracks in three-dimensional finite bodies, *Fract. Mech. Fourteenth Symp. I Theory Anal.* ASTM STP791. (1983).
  - [34] S. Biroasca, J.Y. Buffiere, F.A. Garcia-Pastor, M. Karadge, L. Babout, M. Preuss, Three-dimensional characterization of fatigue cracks in Ti-6246 using X-ray tomography and electron backscatter diffraction, *Acta Mater.* 57 (2009) 5834–5847. doi:10.1016/j.actamat.2009.08.009.
  - [35] J.T. Burns, V.K. Gupta, S.R. Agnew, R.P. Gangloff, Effect of low temperature on fatigue crack formation and microstructure-scale propagation in legacy and modern Al-Zn-Mg-Cu alloys, *Int. J. Fatigue.* 55 (2013) 268–275. doi:10.1016/j.ijfatigue.2013.06.025.
  - [36] T. Vojtek, A. Hohenwarter, R. Pippan, J. Pokluda, Experimental evidence of a common local mode II growth mechanism of fatigue cracks loaded in modes II, III and II + III in niobium and titanium, *Int. J. Fatigue.* 92 (2016) 470–477. doi:10.1016/j.ijfatigue.2016.02.042.